WAVELET-BASED COMPRESSED SENSING
FOR POLARIMETRIC SAR TOMOGRAPHY

Esteban Aguilera, Matteo Nannini, and Andreas Reigber

Microwaves and Radar Institute, German Aerospace Center (DLR)
P.O. Box 1116, 82230 Wessling, Germany

ABSTRACT

Tomographic synthetic aperture radar (SAR) imaging has been recently formulated in a wavelet-based compressed sensing (CS) framework. This paper reviews the underlying sparsity-driven algorithms for single-channel as well as polarimetric tomography, and discusses its applicability in terms of ambiguity rejection, physical validity, acquisition geometry, and required *a priori* knowledge. In addition, we present a comparison with traditional non-parametric spectral estimators by using L-band data acquired by the Experimental SAR (E-SAR) sensor of the German Aerospace Center (DLR).

Keywords: Compressed sensing (CS); forest structure; synthetic aperture radar (SAR) tomography; wavelets.

1. INTRODUCTION

With the advent of nonlinear spectral estimators, tomographic artifacts due to unfavorable sampling conditions have been substantially mitigated. In fact, these methods have allowed for super-resolution imaging not only with a limited number of baselines but also with nonideal acquisition geometries. Cases in point are the well-known adaptive [1–4] and subspace-based spectral estimators [5–7, 4, 8]. Additional examples include the singular-value decomposition (SVD) method [9], along with its variants [10]. Alternative approaches have focused on estimating the backscattered power and scattering center of different scattering mechanisms by extending the concept of synthetic aperture radar (SAR) interferometry [11]. Also, compressed sensing (CS) inversion techniques have been recently adapted for SAR tomography [12–17]. This paper reviews the mechanics together with experimental results of two of these CS methods, in particular those based on wavelet expansions [16, 17] (from now on referred to as WCS methods), and discusses their applicability to forested areas in terms of ambiguity rejection, physical validity, acquisition geometry, and required *a priori* knowledge.

2. WCS FOR SAR TOMOGRAPHY

For the sake of simplicity, we will first restructure the conventional multibaseline model. To this end, let $C^{i,j} \in \mathbb{C}^{M \times M}$ be the multibaseline covariance matrix resulting from M parallel passes [18, 19] and two polarimetric channels i and j at a specific azimuth–range position, with $1 \leq i,j \leq 3$. For example, i and j could denote the hh and hv channels, respectively. Also, let $A \in \mathbb{C}^{M \times N}$ denote a steering or sensing matrix, obtained by computing the phase rotations due to the distance between M sensor positions and N targets distributed along the cross-range direction [6]. Then, we can define $c^{i,j} = vec(C^{i,j}) \in \mathbb{C}^{M^2}$ (column-major vectorization) and the functions $to\_row(\cdot)$ and $to\_col(\cdot)$, which take a linear index corresponding to $c^{i,j}$ as an argument and return the row and column indices corresponding to $C^{i,j}$, respectively. Consequently, if we let X_k indicate the row of any matrix X, we can construct $\Phi \in \mathbb{C}^{M^2 \times N}$ by computing

$$\Phi_\ell = A_{to\_row(\ell)} \odot conj(A_{to\_col(\ell)}) \qquad (1)$$

for all $1 \leq \ell \leq M^2$, where $\odot$ indicates element-wise multiplication. Note that the remainder of Section 2 will build only upon $c^{i,j}$ and Φ.

2.1. Single-Channel WCS

As thoroughly developed in [16], the WCS reconstruction of the cross-range power distribution $p \in \mathbb{R}_{\geq 0}^N$, for a specific polarimetric channel i, can be carried out directly as follows:

$$\min_{\widetilde{p}} \; \|\Psi \widetilde{p}\|_1 \text{ subject to } \left\|\Phi \widetilde{p} - c^{i,i}\right\|_2 \leq \varepsilon \qquad (2)$$

where $\Psi \in \mathbb{R}^{N \times N}$ is a suitable wavelet basis and ε can be used to control the trade-off between sparsity in Ψ and model mismatch. In accordance with the definition of p, the optimization has to be carried out over the set of nonnegative real numbers.

2.2. Polarimetric WCS

When either dual-polarized or fully polarimetric measurements are available, the WCS reconstruction not only provides the backscattered power for each channel but also is able to recover polarimetric statistics for a specific cross-range position [17]. The basic method proceeds as follows:

1) Construct $D \in \mathbb{C}^{M^2 \times 9}$ such that

$$D = [\begin{array}{cccc} c_{1,1} & c_{2,1} & \cdots & c_{3,3} \end{array}] \quad (3)$$

2) Compute the best rank-2 approximation of D by means of the SVD and denote it D^2.

3) Take the adjoint of the resulting right singular vectors and form $V \in \mathbb{C}^{2 \times 9}$.

4) Perform the following optimization

$$\min_{\widetilde{\beta}} \left\| \widetilde{\beta} \right\|_{2,1} \text{ subject to } \left\| \Phi \Psi^T \widetilde{\beta} V - D^2 \right\|_F \leq \varepsilon \quad (4)$$

where $\beta \in \mathbb{R}^{N \times 2}$, $\Psi \in \mathbb{R}^{N \times N}$ is a wavelet basis, and ε is an upper bound on the model mismatch. Also, suitable constraints should be added in order to ensure that every row of $\Psi^T \widetilde{\beta} V$ (when rearranged in a 3-by-3 matrix) results in a positive-semidefinite matrix (see [17] and the references therein).

5) Compute $\widetilde{Z} = \Psi^T \widetilde{\beta} V$.

The output of this algorithm is then $\widetilde{Z} \in \mathbb{C}^{N \times 9}$, and thus provides second-order polarimetric statistics for N cross-range positions, which can be reshaped into the well-known 3-by-3 coherency matrix [20].

3. EXPERIMENTAL RESULTS

For analysis purposes, we used fully polarimetric multi-baseline L-band data acquired by the Experimental SAR (E-SAR) airborne sensor of DLR during a campaign near Dornstetten, Germany, in 2006. Twenty-one passes were performed at approximately the same altitude with horizontal baselines of about $20\,\mathrm{m}$. The center frequency used was $1.3\,\mathrm{GHz}$ and the nominal altitude above ground was about $3200\,\mathrm{m}$ [19]. The resolutions were $0.66\,\mathrm{m}$ and $2.07\,\mathrm{m}$ in azimuth and range, respectively. Also, two different constellations were considered (see Fig. 1) employing: *C1*) all 21 passes and *C2*) a subset of these consisting of 10 irregular passes.

3.1. Single-Channel WCS Experiments

First, we selected contiguous azimuth positions at a range distance of $4501.61\,\mathrm{m}$ and took a $4 \times 14\,\mathrm{m}^2$ azimuth–range window. As a result, we obtained tomographic
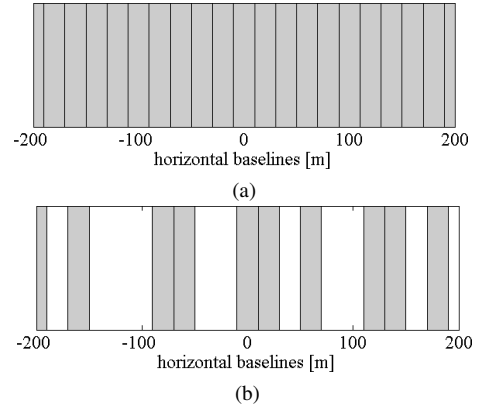

Figure 1. Horizontal baseline distribution for: (a) all 21 passes, and (b) a subset consisting of 10 passes

slices as a function of azimuth and height of dimensions $176\,\mathrm{m}$ by $40\,\mathrm{m}$, respectively. In Fig. 2, we used Fourier beamforming. Fig. 2a and 2b display the normalized sum of the power distribution throughout polarimetric channels using constellations *C1* and *C2*, respectively. Likewise, as presented in Fig. 3, we carried out the reconstruction with Capon's beamformer. Alternatively, Fig. 4 shows the results obtained using a variant of single-channel WCS (see equation (16) in [16]) based on $c^{span} = c^{1,1} + c^{2,2} + c^{3,3}$ so as to directly recover the polarimetric span [16]. The wavelet basis corresponded to a Daubechies Symmlet wavelet with 4 vanishing moments and 3 levels of decomposition.

3.2. Polarimetric WCS Experiments

Lastly, for the polarimetric WCS case, we selected several azimuth positions at a range distance of $4816.30\,\mathrm{m}$ and computed the covariance matrices $c^{i,j}$ for all $1 \leq i,j \leq 3$ by taking a $20 \times 20\,\mathrm{m}^2$ estimation window. Accordingly, we obtained slices as a function of azimuth and height of dimensions $300\,\mathrm{m}$ by $40\,\mathrm{m}$, respectively. Fig. 5 shows the normalized reconstructed profiles for the hh, vv, and hv channels using constellation *C2* and a conventional Fourier inversion of the rearranged rank-2 approximation of D in (3). Fig. 6 presents tomograms found by the polarimetric WCS method using the same wavelet basis as in Section 3.1

4. DISCUSSION

The tomograms shown in this paper, which are in line with the analysis reported in [16, 17], emphasize the ambiguity-rejection capabilities of WCS as well as its ability to recover the complete cross-range power distribution with few highly irregular passes. A direct (and desirable) result is the increase in the height of ambiguity (see Fig. 4). In addition, the polarimetric WCS method provides high resolution while attaining physical validity (in terms of positive semidefiniteness), a property that is
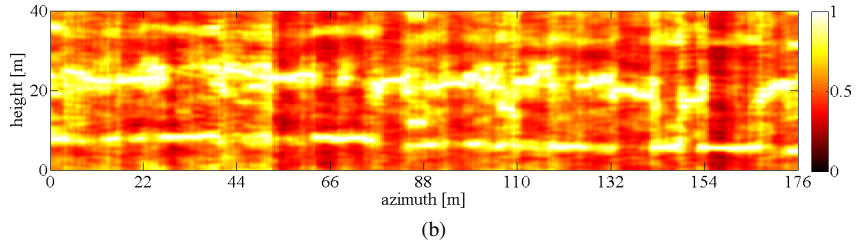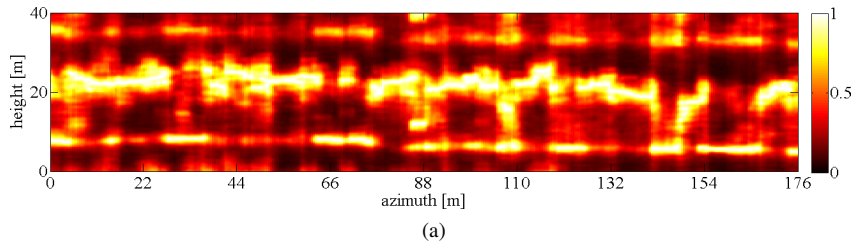
Figure 2. Span of tomogram obtained by Fourier beamforming as a function of azimuth and height (176 m by 40 m) using a $4 \times 14\,m^2$ window with: (a) 21 and (b) 10 passes. Range distance: 4501.61 m.

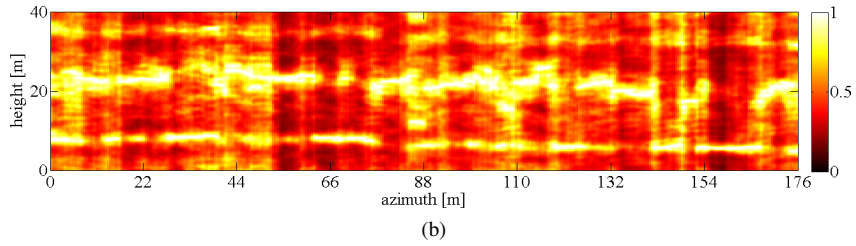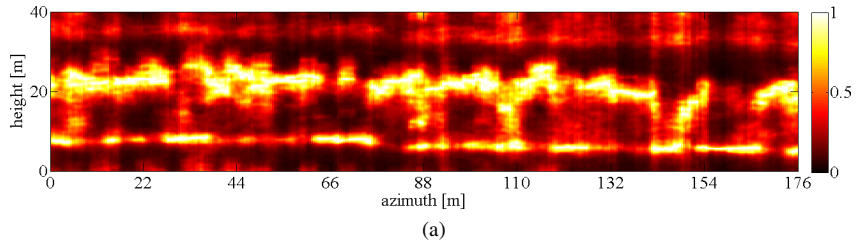*Figure 3. Span of tomogram obtained by Capon's method as a function of azimuth and height (176 m by 40 m) using a $4 \times 14\,m^2$ window with: (a) 21 and (b) 10 passes. Range distance: 4501.61 m.*

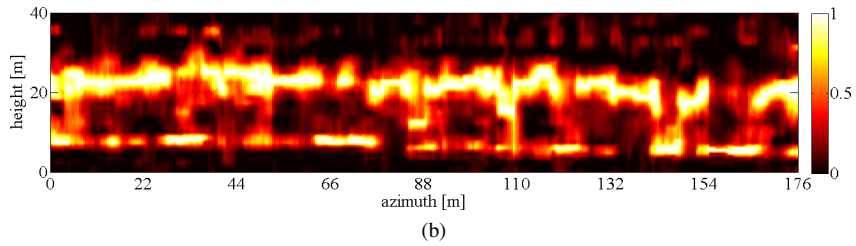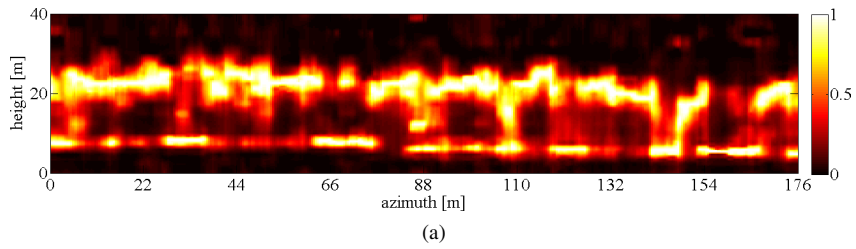*Figure 4. Span of tomogram obtained by single-channel WCS as a function of azimuth and height (176 m by 40 m) using a $4 \times 14\,m^2$ window with: (a) 21 and (b) 10 passes. Range distance: 4501.61 m.*
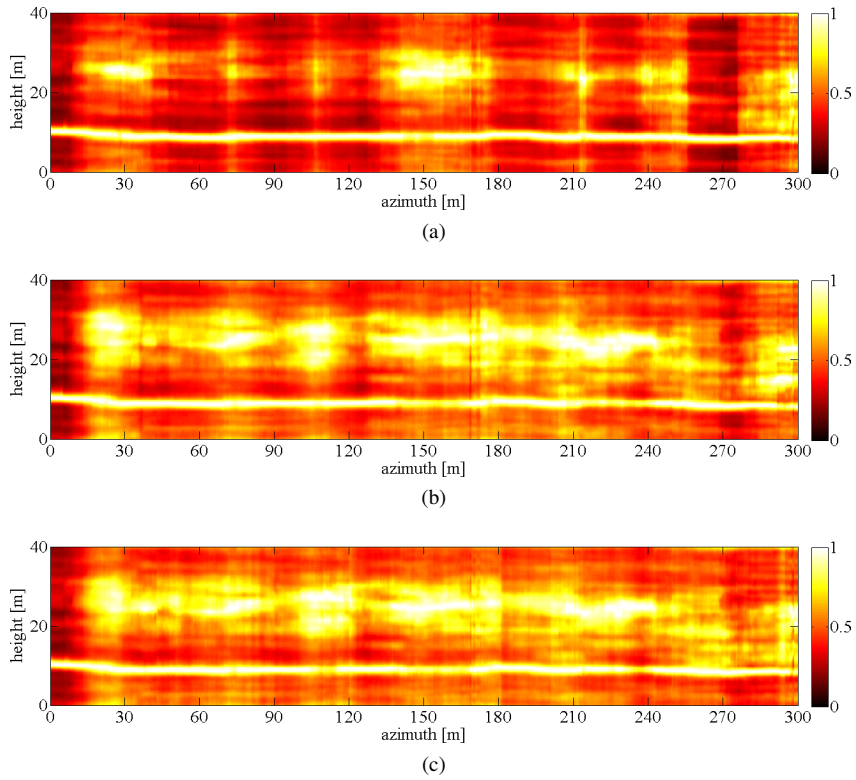
Figure 5. Tomographic slices in the (a) hh, (b) vv, and (c) hv channels (300 m by 40 m) obtained by a conventional Fourier inversion using a $20 \times 20\,m^2$ window and 10 passes. Range distance: 4816.30 m.
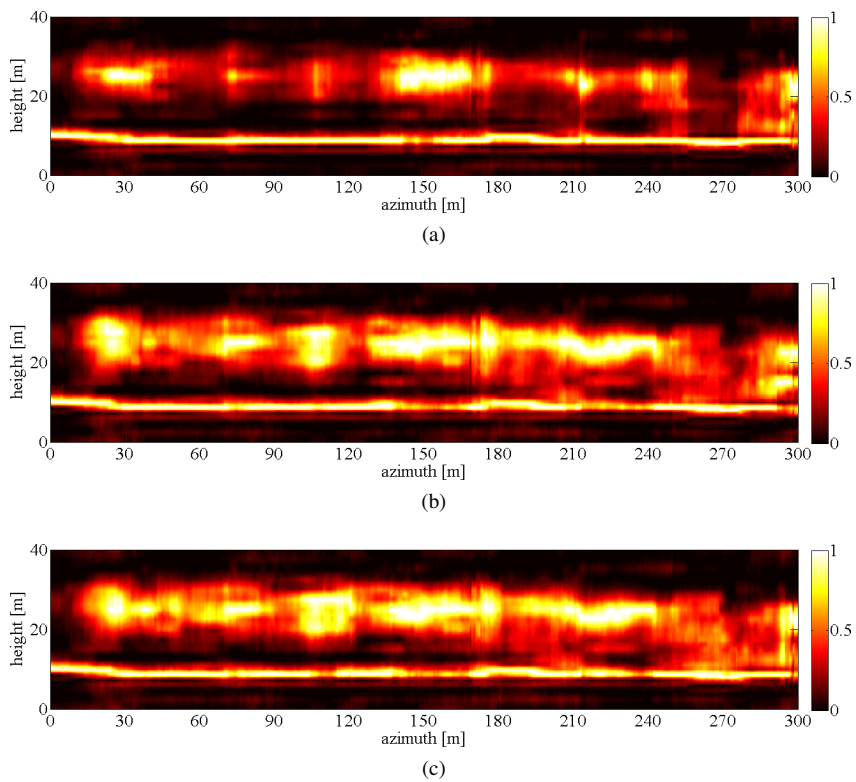

Figure 6. Tomographic slices in the (a) hh, (b) vv, and (c) hv channels (300 m by 40 m) obtained by the polarimetric WCS method using a $20 \times 20\,m^2$ window and 10 passes. Range distance: 4816.30 m.

commonly sacrificed by most super-resolution estimators. Nevertheless, special consideration should be given to the following points:

1) A reduction in aliasing-like artifacts entails a nondeterministic acquisition geometry [16], which might require extensive simulations prior to planning campaigns that rely on very few baselines. This downside could be alleviated by having a large tomographic aperture with a few small approximately regular baselines, in addition to few large highly irregular ones. Nonetheless, when several passes are available, the natural deviations from the ideal tracks seem to provide the required randomness for ambiguity rejection (see, for example, Fig. 4a).

2) Large tomographic apertures with very sparse baselines can reduce the usable swath [16], since the vertical wavenumber at the near range intrinsically experiences higher variations [21]. Hence, this kind of sparse constellation and wide-swath airborne tomography are bound to be conflicting requirements, unless simpler models that make additional assumptions are used.

3) As WCS inherently estimates the cross-range backscattered power simultaneously for all heights in a defined observation space, it is important to choose an appropriate range of heights. However, this *a priori* knowledge is also implicitly critical for conventional estimators, as the maximum height is an important parameter for appropriate campaign design [19].

REFERENCES

[1] F. Lombardini and A. Reigber. Adaptive spectral estimation for multibaseline SAR tomography with airborne L-band data. *Proc. IGARSS*, 3:2014–2016, Jul. 2003.

[2] F. Lombardini, M. Pardini, G. Fornaro, F. Serafino, L. Verrazzani, and M. Costantini. Linear and adaptive spaceborne three-dimensional SAR tomography: a comparison on real data. *IET Radar, Sonar & Navigation*, 3(4):424–436, Jun. 2009.

[3] S. Sauer, L. Ferro-Famil, A. Reigber, and E. Pottier. Three-dimensional imaging and scattering mechanism estimation over urban scenes using dual-baseline polarimetric InSAR observations at L-band. *IEEE Trans. Geosci. Remote Sens.*, 49(11):4616–4629, Jun. 2011.

[4] O. Frey and E. Meier. 3-D time-domain SAR imaging of a forest using airborne multibaseline data at L- and P-Bands. *IEEE Trans. Geosci. Remote Sens.*, 49(10):3660–3664, Oct. 2011.

[5] S. Guillaso and A. Reigber. Polarimetric SAR Tomography. *Proc. of POLINSAR*, Jan. 2005.

[6] M. Nannini, R. Scheiber, and A.Moreira. Estimation of the minimum number of tracks for SAR tomography. *IEEE Trans. Geosci. Remote Sens.*, 47:531–543, Feb. 2009.

[7] Y. Huang, L. Ferro-Famil, and A. Reigber. Under-foliage object imaging using SAR tomography and polarimetric spectral estimators. *IEEE Trans. Geosci. Remote Sens.*, 50(6):2213–2225, Jun. 2012.

[8] O. Frey and E. Meier. Analyzing tomographic SAR data of a forest with respect to frequency, polarization, and focusing technique. *IEEE Trans. Geosci. Remote Sens.*, 49(10):3648–3659, Oct. 2011.

[9] F. Serafino G. Fornaro and F. Soldovieri. Three-dimensional focusing with multipass SAR data. *IEEE Trans. Geosci. Remote Sens.*, 41(3):507–517, Mar. 2003.

[10] X.X. Zhu and R. Bamler. Very high resolution spaceborne SAR tomography in urban environment. *IEEE Trans. Geosci. Remote Sens.*, 48(12):4296–4308, Dec. 2010.

[11] S. Tebaldini. Single and multipolarimetric SAR tomography of forested areas: A parametric approach. *IEEE Trans. Geosci. Remote Sens.*, 48(5):2375–2387, May. 2010.

[12] X.X. Zhu and R. Bamler. Tomographic SAR inversion by L1-norm regularization - The compressive sensing approach. *IEEE Trans. Geosci. Remote Sens.*, 48:3839–3846, Oct. 2010.

[13] A. Budillon, A. Evangelista, and G. Schirinzi. Three-dimensional SAR focusing from multipass signals using compressive sampling. *IEEE Trans. Geosci. Remote Sens.*, 49(1):488–499, Jan. 2011.

[14] X.X. Zhu and R. Bamler. Super-resolution power and robustness of compressive sensing for spectral estimation with application to spaceborne tomographic SAR. *IEEE Trans. Geosci. Remote Sens.*, 50(1):247–258, Jan. 2012.

[15] E. Aguilera, M. Nannini, and A. Reigber. Multisignal compressed sensing for polarimetric SAR tomography. *IEEE Geosci. Remote Sens. Lett.*, 8(5):871–875, Sept. 2012.

[16] E. Aguilera, M. Nannini, and A. Reigber. Wavelet-based compressed sensing for SAR tomography of forested areas. *IEEE Trans. Geosci. Remote Sens.*, 2013, in press.

[17] E. Aguilera, M. Nannini, and A. Reigber. A data-adaptive compressed sensing approach to polarimetric SAR tomography of forested areas. *IEEE Geosci. Remote Sens. Lett.*, 10(3):543–547, May 2013.

[18] F. Gini, F. Lombardini, and M. Montanari. Layover solution in multibaseline sar interferometry. *IEEE Trans. Aerosp. Electron. Syst.*, 38(4):1344–1356, Oct. 2002.

[19] M. Nannini, R. Scheiber, R. Horn, and A.Moreira. First 3-D reconstructions of targets hidden beneath foliage by means of polarimetric SAR tomography. *IEEE Geosci. Remote Sens. Lett.*, PP(99):1–5, Jul. 2011.

[20] S. Cloude and E. Pottier. A review of target decomposition theorems in radar polarimetry. *IEEE Trans. Geosci. Remote Sens.*, 34(2):498–518, Mar. 1996.

[21] R. Bamler and P. Hartl. Synthetic aperture radar interferometry. *Inverse Problems*, 14(4):1–54, Aug. 1998.